metals

MDPI

Article

Determining Hot Deformation Behavior and Rheology Laws of Selected Austenitic Stainless Steels

Josef Němec [1], Lenka Kunčická [1,2,*], Petr Opěla [1] and Karel Dvořák [3]

[1] Department of Metallurgical Technologies, Faculty of Materials Science and Technology, VŠB–Technical University of Ostrava, 17. Listopadu 2172/15, 70800 Ostrava, Czech Republic; petr.opela@vsb.cz (P.O.)
[2] Institute of Physics of Materials, Czech Academy of Sciences, Žižkova 22, 61600 Brno, Czech Republic
[3] Faculty of Civil Engineering, Brno University of Technology, Veveří 331/95, 60200 Brno, Czech Republic
* Correspondence: kuncicka@ipm.cz

Abstract: Due to their versatile properties, austenitic stainless steels have a wide application potential, including in specific fields, such as the nuclear power industry. ChN35VT steel is a chromium–nickel–tungsten type of steel stabilized by titanium, and it is suitable for parts subjected to considerable mechanical stress at elevated temperatures. However, the available data on its deformation behavior at elevated/high temperatures is scarce. The core of the presented research was thus the experimental characterization of the deformation behavior of the ChN35VT steel under hot conditions via the determination of flow stress curves, and their correlation with microstructure development. The obtained data was further compared with data acquired for 08Ch18N10T steel, which is also known for its applicability in the nuclear power industry. The experimental results were subsequently used to determine the Hensel-Spittel rheology laws for both the steels. The ChN35VT steel exhibited notably higher flow stress values in comparison with the 08Ch18N10T steel. This difference was more significant the lower the temperature and the higher the strain rate. Considering the peak stress values, the lowest difference was ~8 MPa (1250 °C and 0.01 s^{-1}), and the highest was ~150 MPa (850 °C and 10 s^{-1}). These findings also corresponded to the microstructure developments—the higher the deformation temperature, the more negligible the observed differences as regards the grain size and morphology.

Keywords: austenitic stainless steel; deformation behavior; Hensel-Spittel; microstructure

check for updates

Citation: Němec, J.; Kunčická, L.; Opěla, P.; Dvořák, K. Determining Hot Deformation Behavior and Rheology Laws of Selected Austenitic Stainless Steels. *Metals* **2023**, *13*, 1902. https://doi.org/10.3390/met13111902

Academic Editor: Qingsong Mei

Received: 21 October 2023
Revised: 12 November 2023
Accepted: 16 November 2023
Published: 17 November 2023

1. Introduction

Due to their high corrosion resistance, favorable heat resistance, and other advantageous properties, stainless steels are used in a wide range of industries [1,2]. They are especially favorable for demanding applications [3,4]. For example, stainless steels are used in the healthcare sector for instruments [5,6], implants [7,8], or stents [9–11]; in energetics for hydrogen storage tanks [12]; or pipes for the transportation of fluids containing chloride ions in solar power plants [13]; in nuclear technology applications [14,15]; as well as for the blades of gas turbines [16,17]; combustion chambers [18,19]; fuel cells [20], etc.

The ChN35VT and 08Ch18N10T austenitic stainless steels (the first mentioned is equivalent to the H23020 steel type, while the latter is equivalent to the AISI 321 steel type) are both alloyed with high volumes of nickel and chromium, and stabilized with titanium. Due to the significant volume fraction of the alloying elements, the steels typically feature high volumes of grain boundary precipitates, such as complex carbides of Cr, Fe, Mn, Ni, and Ti [21], or titanium carbonitrides [22]. As titanium is a powerful carbide-forming element, it preferentially binds carbon and thereby advantageously reduces the probability of the formation of undesirable $(Fe, Cr)_{23}C_6$ carbides, which negatively affect the material properties in the temperature range of 400–800 °C [23,24]. The formation of $Cr_{23}C_6$ carbides at grain boundaries reduces the amount of dissolved chromium, thereby decreasing the corrosion resistance [25,26]. Titanium does not only react with carbon and nitrogen to produce

carbonitrides [27], but also decreases the susceptibility to intergranular stress corrosion cracking by minimizing chromium carbide precipitation along the grain boundaries [28], and effectively suppresses recrystallization during forming [29], all of which enhances the mechanical properties and increases the lifetime of the final products [30,31]. Compared to 08Ch18N10T steel, the corrosion resistance of ChN35VT steel is even more enhanced by the addition of ~3 wt.% of tungsten [32]. Another difference between these two steels that is worth mentioning is the nickel content, which is significantly higher for ChN35VT steel (~36 wt.% compared to ~11 wt.% for the 08Ch18N10T steel) [33]. Nevertheless, the available literature sources on the mechanical behavior of ChN35VT steel, especially at elevated and hot temperatures, and moreover in correlation with structure development, are scarce.

Austenitic steels are typically produced in electric arc furnaces and subsequently cast via continuous casting in the form of blocks, slabs, or, in special cases, in molds [34]. The blanks of such steels can be further processed using conventional methods of plastic deformation, such as rolling [35,36]—for example, sheets of 08Ch18N10T steel are typically rolled under hot, and, subsequently, cold conditions [37]—drawing (tubes [38,39]), or forging [24]. However, non-conventional methods [40], e.g., rotary swaging [41–44], modified rolling processes [45,46], or methods of severe plastic deformation (SPD), such as various types of the equal channel angular pressing (ECAP) method, [47–53], can also be used. Last but not least, austenitic stainless steels have recently been a subject of additive manufacturing (3D printing) [54–57], possibly in combination with other deformation processes, which can advantageously affect the final properties of as-built materials [58,59].

The main aim of this research was to examine the hot deformation behavior of the above-discussed ChN35VT steel. As far as the authors' knowledge reaches, this topic has not been sufficiently researched so far. The examination is performed via the evaluation of experimentally acquired flow stress data, characterized in a wide range of thermo-mechanical conditions. The data on the mechanical behavior was further correlated with corresponding microscopic analyses. In addition, the acquired data was processed by a nonlinear regression analysis with the application of the Hensel-Spittel rheological law, which resulted in the development of a flow stress prediction that can further be used to enhance the material databases of FEM simulation software. In order to validate the results acquired for the ChN35VT steel, a comparison with another steel used in the nuclear power industry, i.e., the mentioned 08Ch18N10T stainless steel, was finally performed.

2. Materials and Methods

2.1. Experimental Material

Both the ChN35VT and 08Ch18N10T steels investigated in this research were produced and supplied by ZDAS, a. s. (ZDAS, a. s., Žďár and Sázavou, Czech Republic). These steels feature different chemical compositions, primarily as regards the Ni content—see Table 1 summarizing the chemical compositions of the steels. Both the austenitic stainless steels were produced in electric arc furnaces, cast into ingots, and deformation processed by rolling under hot conditions into bars with ~12.3 mm in diameter; see the mechanical properties of the delivered steel bars in Table 2. The bars were then machined into testing specimens with the final diameter of 10 mm and length of 15 mm.

Table 1. Comparison of chemical compositions of investigated stainless steels (contents in wt.%).

Steel Type	Ni	Cr	W	Mn	Ti	Si	S	P	C
ChN35VT	34–38	13.5–16.5	2.7–3.7	1–2	1.2–1.9	<0.8	<0.03	<0.045	<0.12
08Ch18N10T	9.5–12.0	17.0–19.0		<2	>5x%C	<10	<0.03	<0.045	<0.10

Table 2. Comparison of mechanical properties of investigated stainless steels.

Steel Type	$Rp_{0,2}$ [MPa]	Rm [MPa]	A [%]	KCU (RT) [J/cm^2]
ChN35VT	392	735	15	59
08Ch18N10T	195	550–750	35	80

2.2. Hot Compression Testing

The deformation behavior of the ChN35VT steel at elevated and hot temperatures was investigated via evaluation of the development of flow stress under various thermo-mechanical conditions. To acquire the required flow stress data, hot uniaxial compression tests were performed under six individual deformation temperatures (850, 900, 970, 1060, 1150, and 1250 °C), and four strain rates (0.01, 0.1, 1, and 10 s^{-1})—i.e., 24 tests were performed in total. For the purposes of comparison of the acquired data with another steel commonly applied in the nuclear power industry, 08Ch18N10T (AISI 321) steel was tested, too. However, since the behavior of 08Ch18N10T steel has already been well-researched (e.g., [60–63]), the testing was performed only under selected conditions—see Table 3.

Table 3. Examined hot compression test conditions: ChN35VT (a) and 08Ch18N10T (b).

T (°C)/$\dot{\varepsilon}$ (s^{-1})	0.01	0.1	1	10
850	a	a	a	a
900	a	a, b	a, b	a, b
970	a	a	a	a
1060	a, b	a, b	a, b	a, b
1150	a	a	a	a
1250	a	a	a,b	a

The hot compression tests were performed using the above described machined cylindrical samples. Each sample was subjected to the following testing procedure: The required deformation temperature was achieved via direct electric resistance heating with a heating rate of 5 °C·s^{-1}. Before performing the deformation, a dwell time of 300 s on the selected temperature was applied. Temperature control was mediated via a pair of thermocouple wires of K-type (i.e., Ni–Cr (+) and Ni–Al (−)), and R-type (Pt–13%Rh (+) and Pt (−)) for the temperatures of 850 °C to 1150 °C, and the temperature of 1250 °C, respectively. The thermocouples were welded on the surfaces of the testing samples (in the middle length). The compressive deformation was realized up to the true strain value of −1.1 to ensure sufficient reliability of the data up to the true (logarithmic) strain of −1.0. Each of the deformed samples was then quenched for 60 s by pressurized air. The testing chamber was held under vacuum until the quenching stage to prohibit any development of oxidation processes. The sample–anvil interface was treated by tantalum foils in combination with a nickel-based high-temperature grease to decrease friction forces and inhibit anvil wear during testing. The described procedure was performed with the use of the Gleeble®Thermal-Mechanical Simulator equipped with the Hydrawedge testing unit (Dynamic Systems Inc., Poestenkill, NY, USA).

2.3. Structure Analyses

Having performed the compression testing, selected characteristic samples were subjected to subsequent structure observations. These were performed on cross-sectional cuts from the deformed testing samples. The analyses were carried out using scanning electron microscopy (SEM); a Tescan Lyra 3 XMU FEG/SEMxFIB microscope (Tescan Orsay Holding a.s., Brno, Czech Republic) equipped with a Symmetry EBSD detector (Oxford Instruments, Abingdon, UK) was used for these purposes. The samples for the SEM-EBSD analyses were prepared by manual grinding on SiC papers, subsequent manual polishing, and final electrolytic polishing. The scanned area was 150 × 150 μm^2 for each sample,

and the scan step was 0.2 µm. The acquired microstructure data was evaluated using the AZtecCrystal software (https://nano.oxinst.com/azteccrystal, accessed on 15 November 2023, Oxford Instruments, Abingdon, UK). The limits for the grains and grain boundaries considered during the evaluations were 5° for LAGB (low-angle grain boundaries), and 15° for HAGB (high-angle grain boundaries).

2.4. Calculating the Rheology Law

Bearing in mind various approaches to assemble a suitable rheology model to characterize the deformation behavior of metallic materials, see, e.g., [64,65], the Hensel-Spittel rheology law (Equation (1)) [66–68] was selected to describe the relationship between the flow curve predictors (i.e., temperature, strain rate, and true strain), and corresponding outcome (i.e., true flow stress):

$$\sigma = A \cdot \mathrm{e}^{m_1 \cdot T} \cdot T^{m_9} \cdot \varepsilon^{m_2} \cdot \mathrm{e}^{m_4/\varepsilon} \cdot (1+\varepsilon)^{m_5 \cdot T} \cdot \mathrm{e}^{m_7 \cdot \varepsilon} \cdot \dot{\varepsilon}^{m_3} \cdot \dot{\varepsilon}^{m_8 \cdot T} \quad (1)$$

where T (°C), $\dot{\varepsilon}$ (s^{-1}), ε (−), and σ (MPa) are deformation temperature, strain rate, true strain, and true flow stress, respectively, A, m_1, m_2, m_3, m_4, m_5, m_7, m_8, and m_9 are material parameters, and e (−) is Euler's number. The material parameters were established via the method of nonlinear least squares, with the application of the Levenberg–Marquardt optimization algorithm [69,70] (performed using the GNU Octave-4.2.1 software equipped by the optim-1.5.2 package, free software). The algorithm uses an initial estimate of material parameters (usually taken from a previous regression analysis) and iteratively refines this estimate to find the most precise fit with the experimentally acquired hot compression data. In other words, the algorithm attempts to find parameters for which Equation (1) provides the lowest possible value of a fitness function (a sum of squared errors in this case). The refining of the initial estimate via iteration algorithms has the following general form (Equation (2)):

$$\beta_{i+1} = \beta_i + \delta \quad (2)$$

where β_i and $\beta_i + 1$ represent $m \times 1$ vector of the material parameters from previous and subsequent iteration step, respectively, m corresponds to the number of material parameters (nine in our case). The $m \times 1$ increment vector δ then contains values for the modification of previous iteration step parameters, and in the case of the Levenberg–Marquardt algorithm, it has the following form (Equation (3)):

$$\delta = -(H + \lambda \cdot \mathrm{diag}[H])^{-1} \cdot \nabla_\beta F \quad (3)$$

where $\nabla_\beta F$ is the $m \times 1$ vector of fitness function gradients. The $m \times m$ Hessian matrix of second-order partial derivatives, H, is then given by multiplication of $m \times n$ transposed Jacobian matrix and $n \times m$ Jacobian matrix containing partial derivatives of the fitness function with respect to the examined material parameters, where n corresponds to the number of observations (datapoints). The λ-parameter is then a damping factor, the value of which is influenced by returned iteration step fitness function value.

3. Results

3.1. Rheology Law

The material parameters, i.e., A and $m_1 - m_9$, established to fit the experimental flow stress curves for both the studied steels, are summarized in Table 3. The suitability of the regression fit of the assembled Hensel-Spittel rheology model is supported by low root mean squared error (*RMSE*) values and high values of the Pearson correlation coefficient (R)—see Table 4. A graphical comparison of the numerically acquired data with the experimentally acquired ones is also offered in Section 3.2.

Table 4. Hensel-Spittel rheology law parameters.

Parameter	ChN35VT	08Ch18N10T
A	0.11849	165,812,128.83665
m_1	−0.00520	−0.00131
m_2	0.26891	0.17785
m_3	−0.22211	−0.36327
m_4	−0.00472	−0.02081
m_5	−0.00128	−0.00113
m_7	0.12993	0.29098
m_8	0.00034	0.00047
m_9	1.94258	−1.74049
RMSE (MPa)	14.30052	8.40329
R	0.99238	0.99307

3.2. Deformation Behavior

Figure 1a–f show the flow stress curves (stress–strain curves) for the ChN35VT steel acquired experimentally at the temperatures of 850, 900, 970, 1060, 1150, and 1250 °C, and strain rates of 0.01, 0.1, 1, and 10 s^{-1} (dashed lines). As previously mentioned, these curves were used to assemble the Hensel-Spittel rheological model presented in Section 3.1. In order to demonstrate the model accuracy, the experimental curves showed in Figure 1a–f were supplemented with flow stress curves calculated based on the assembled model (solid lines). Figure 2a–f then show the flow stress (stress–strain) curves for the 08Ch18N10T steel acquired experimentally (dashed lines), and calculated numerically according to the Hensel-Spittel model (solid lines). However, since this steel has been the subject of investigations of various other researchers, we experimentally tested this material only under a limited number of temperature–strain-rate combinations and the experimentally acquired flow stress curves are available only for selected conditions. Nevertheless, this limited number of experimental observations was sufficient to assemble the Hensel-Spittel model, which further enabled the prediction of the flow stress curves also for the conditions, which were not experimentally tested herein (solid lines).

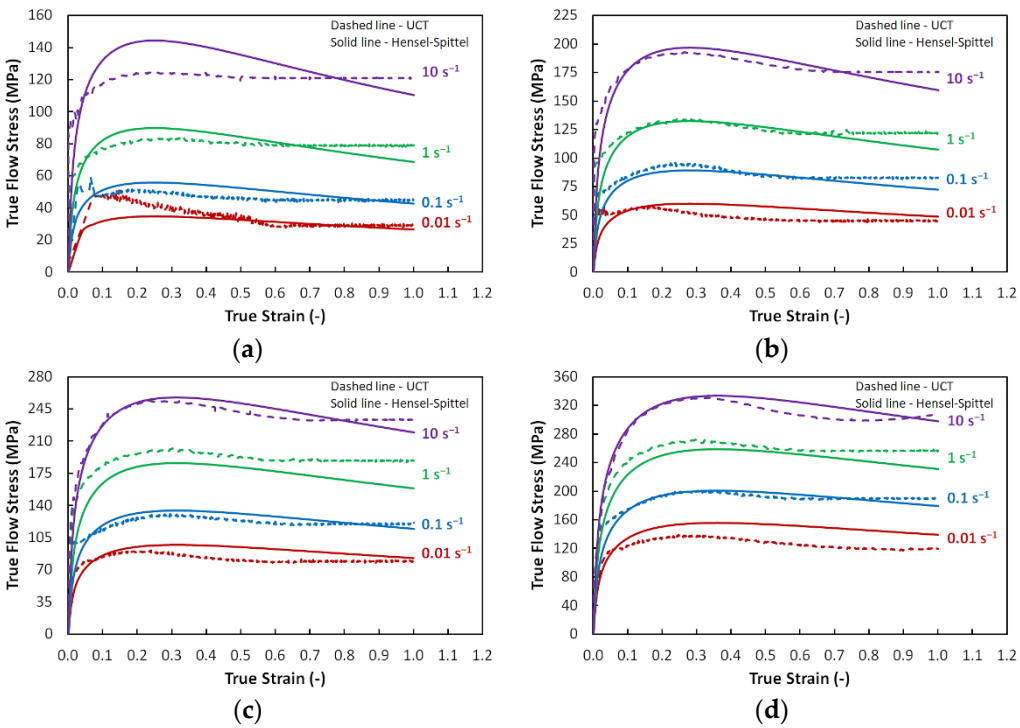

Figure 1. *Cont.*

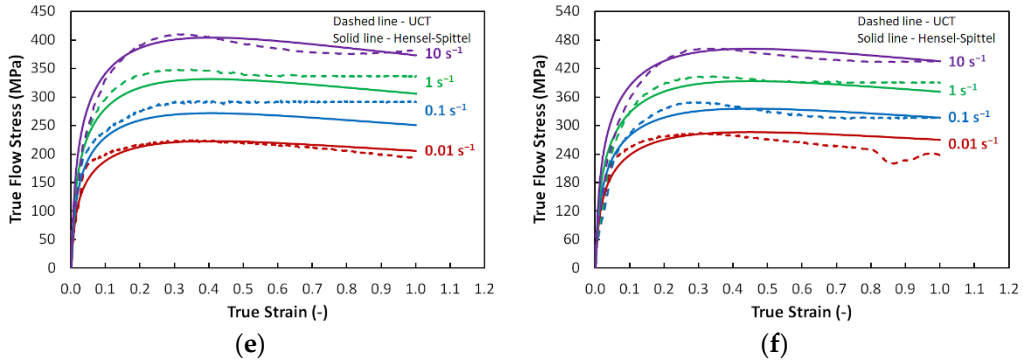

Figure 1. Experimentally acquired and Hensel-Spittel model created flow stress curves for ChN35VT steel: (**a**) 1250 °C; (**b**) 1150 °C; (**c**) 1060 °C; (**d**) 970 °C; (**e**) 900 °C; (**f**) 850 °C.

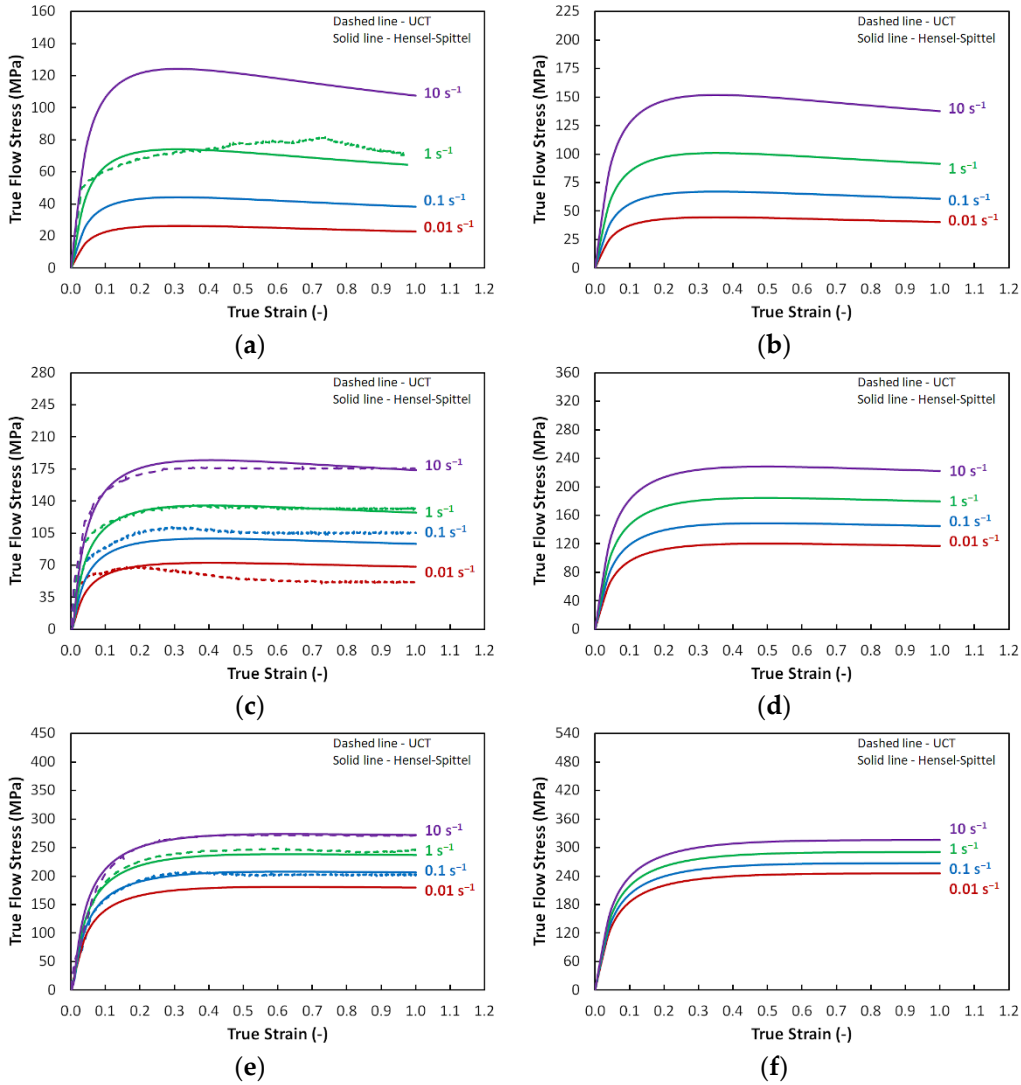

Figure 2. Experimentally acquired and Hensel-Spittel model created flow stress curves for 08Ch18N10T steel: (**a**) 1250 °C; (**b**) 1150 °C; (**c**) 1060 °C; (**d**) 970 °C; (**e**) 900 °C; (**f**) 850 °C.

For both the steels, the higher the temperature and lower the strain rate, the lower the flow stress. As can be seen from the presented figures, the majority of the acquired curves exhibited a flow stress increase up to the peak point, which was directly followed by a steady-state (the flow stress curve acquired experimentally for the ChN35VT steel at 850 °C and 0.01 s^{-1}, Figure 1f, exhibited a local minimum before the end of the test; this

local flow stress decrease could most probably be attributed to an unexpected short-term temperature increase due to a software error). However, exceptions to this were the curves acquired under higher temperatures and lower strain rates, for which a small flow stress decrease followed by a gradual transition to a steady-state after reaching the peak point was observed. Also, the strain rate evidently affected the flow stress values the most at the higher deformation temperatures (1250 °C and 1150 °C). At the lower deformation temperatures, the differences between the flow stress values for the different strain rates were not so striking. This effect was more notable for the ChN35VT steel than for the 08Ch18N10T steel.

When comparing the ChN35VT and 08Ch18N10T steels, it is clear that the flow stress values of the studied ChN35VT steel were significantly higher than those of the 08Ch18N10T steel, under otherwise identical hermos-mechanical conditions. It is also apparent that the lower the temperature, the more significant these differences.

3.3. Microstructure Observations

The microstructure characterization via SEM-EBSD mapping was performed for both the steels, for samples deformed at the temperatures of 900 °C and 1060 °C, and strain rates of 0.1 s^{-1} and 10 s^{-1}. In order to observe the grain morphology, analyses of the band contrast images were performed. Figure 3a,b depict examples of the microstructures acquired for the ChN35VT steel deformed at 1060 °C and 900 °C and at a strain rate of 10 s^{-1}, while Figure 3c,d show the microstructures acquired for the 08Ch18N10T steel deformed at 1060 °C and 900 °C and at a strain rate of 10 s^{-1}. Evidently, the samples of both the steels deformed at the higher temperatures exhibited a rather significant presence of twins, whereas the microstructures of both the steels deformed at the lower temperature featured highly refined grains. Also, the microstructures of the ChN35VT steel generally appeared to be more uniform than those of the 08Ch18N10T steel.

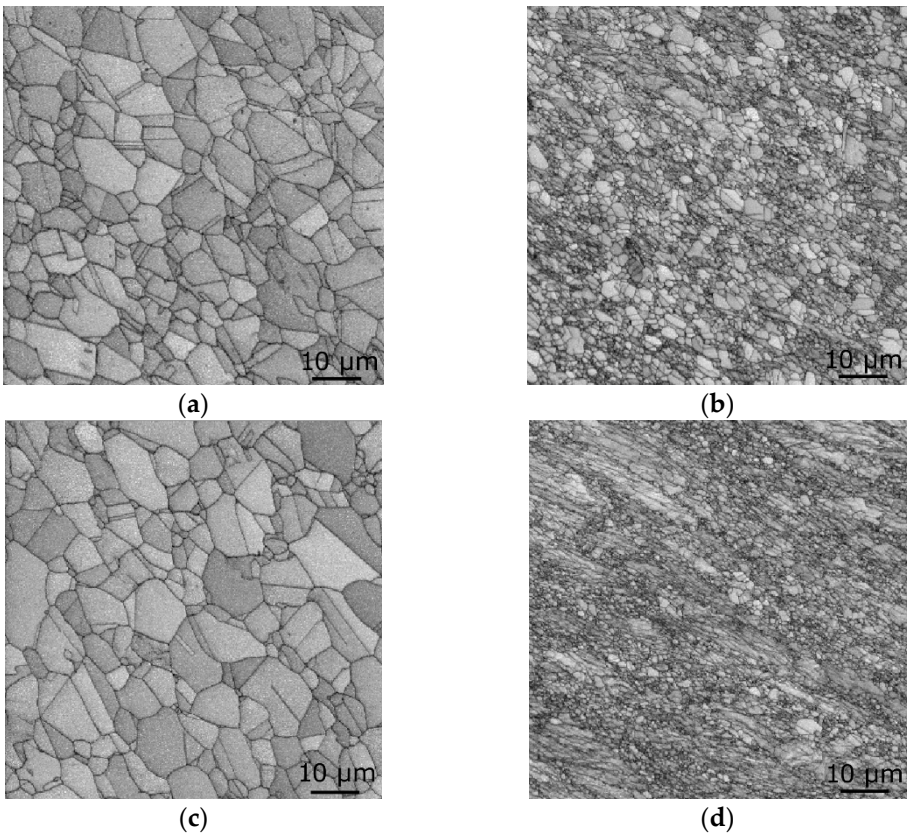

Figure 3. Band contrast images for ChN35VT steel deformed at 1060 °C, 10 s^{-1} (**a**); 900 °C, 10 s^{-1} (**b**); 08Ch18N10T steel deformed at 1060 °C, 10 s^{-1} (**c**); 900 °C, 10 s^{-1} (**d**).

In order to quantify the results and document the effects of the applied hermos-mechanical conditions in greater detail, further microstructure analyses were performed. Figure 4a–d show the results of the analyses of the grain orientations and grain boundaries depicted via the orientation image maps (OIM) for the ChN35VT steel deformed at 1060 °C and 900 °C and at 0.1 s^{-1} and 10 s^{-1}, respectively. Figure 5a–d then correspondingly show the results of such analyses depicted via OIM for the 08Ch18N10T steel. The results of the grain size analyses, depicted by the area-weighted fractions of grain areas in μm^2, for the examined samples are further shown in Figure 4e–h for the ChN35VT steel, and in Figure 5e–h for the 08Ch18N10T steel.

The microstructure observations showed that the ChN35VT steel deformed at higher temperatures exhibited equiaxed grains with more or less random orientations for all the examined strain rates (Figure 4a–c). For the sample deformed at 1060 °C, the average grain size was slightly larger for the lower testing strain rate of 0.1 s^{-1}, i.e., 20.1 μm^2. For the higher strain rate of 10 s^{-1} it was 16.7 μm^2. The sample deformed at the strain rate of 10 s^{-1} featured a higher overall fraction of HAGB (97.3%), although both the samples featured a majority of HAGB (a portion of 84.9% of HAGB was observed within the microstructure of the sample deformed at the strain rate of 0.1 s^{-1}). Also, the fraction of the <111>60° twin boundaries was higher for the sample deformed at the higher strain rate; compared to 31.5% observed for 0.1 s^{-1}, 44.8% was observed for 10 s^{-1}.

On the other hand, the microstructures of the samples deformed at the lower temperature of 900 °C exhibited highly deformed grains at all the examined strain rates (Figure 4b–d). Specifically, the sample deformed at the strain rate of 0.1 s^{-1} exhibited a high fraction of elongated grains, surrounded with small equiaxed grains of more or less random orientations (i.e., necklace-like structure). The HAGB fraction for this sample was 69.5% (compared to a portion of 82.5% of HAGB observed within the microstructure of the 900 °C and 10 s^{-1} sample), and its average grain size was 3.8 μm^2 (although the structure exhibited also larger grains with the areas reaching up to 80 μm^2, see Figure 4f). Increasing the strain rate to 10 s^{-1} contributed to grain fragmentation, the microstructure exhibited a higher fraction of small equiaxed grains, and also a smaller average grain size of 3.0 μm^2. The grain structure was more uniform when compared to the 0.1 s^{-1} sample and the largest grain reached only to less than 50 μm^2, see Figure 4h). The higher strain rate also supported the occurrence of the twinning phenomenon; compared to the 19.9% fraction of <111>60° twin boundaries observed for the 900 °C and 10 s^{-1} sample, there was a negligible occurrence of twin boundaries within the 900 °C and 0.1 s^{-1} sample (4.2%, see Figure 4b).

Similar to the ChN35VT steel, the structure observations of the 08Ch18N10T steel showed that the microstructures of the samples deformed at higher temperatures exhibited equiaxed grains with more or less random orientations at all the examined strain rates (see Figure 5a–c). The average grain size for this steel deformed at the temperature of 1060 °C was slightly larger when compared to the ChN35VT steel deformed at the identical temperature (26.3 μm^2 for the strain rate of 0.1 s^{-1}, and 21.9 μm^2 for the higher strain rate of 10 s^{-1}). However, the applied strain rate imparted significant differences in the fractions of HAGB, and, namely, the fractions of the <111>60° twin boundaries. The HAGB fraction for the 1060 °C and 0.1 s^{-1} 08Ch18N10T steel sample was 62%, 8.2% of which were twin boundaries. On the other hand, the 1060 °C and 10 s^{-1} sample featured a fraction of 93.4% of HAGB, 34.1% of which were twin boundaries.

The morphologies of the grains of the samples processed at the deformation temperature of 900 °C were comparable to those observed within the samples of the ChN35VT steel. However, the grain size was larger for the 08Ch18N10T steel, similar to the samples deformed at 1060 °C. The average grain size of the 900 °C and 0.1 s^{-1} sample was 6.2 μm^2, while for the 900 °C and 0.1 s^{-1} sample it was 8.8 μm^2 (Figure 5f–h). For the 08Ch18N10T steel deformed at 900 °C, both the examined samples exhibited high fractions of elongated grains. The fractions of HAGB in the samples deformed at 0.1 s^{-1} and 10 s^{-1} were 58.9%

and 48%, respectively. The occurrence of twin boundaries within the microstructures of both the 08Ch18N10T steel samples deformed at 900 °C was negligible (Figure 5b–d).

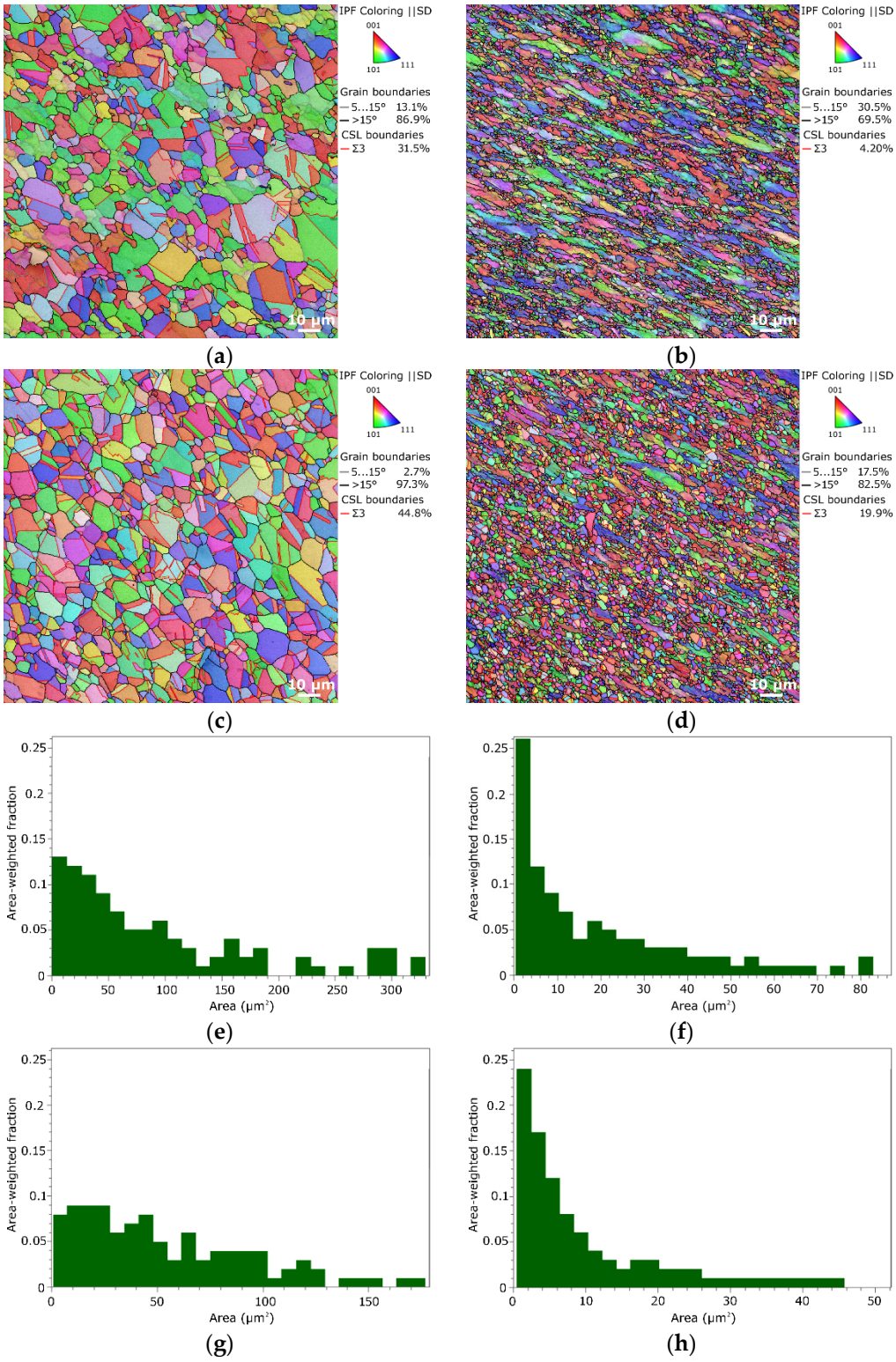

Figure 4. OIM images for ChN35VT steel deformed under specific conditions: 1060 °C, 0.1 s^{-1} (**a**); 900 °C, 0.1 s^{-1} (**b**); 1060 °C, 10 s^{-1} (**c**); 900 °C, 10 s^{-1} (**d**). Grain size depicted via area-weighted grain areas for ChN35VT steel deformed under specific conditions: 1060 °C, 0.1 s^{-1} (**e**); 900 °C, 0.1 s^{-1} (**f**); 1060 °C, 10 s^{-1} (**g**); 900 °C, 10 s^{-1} (**h**).

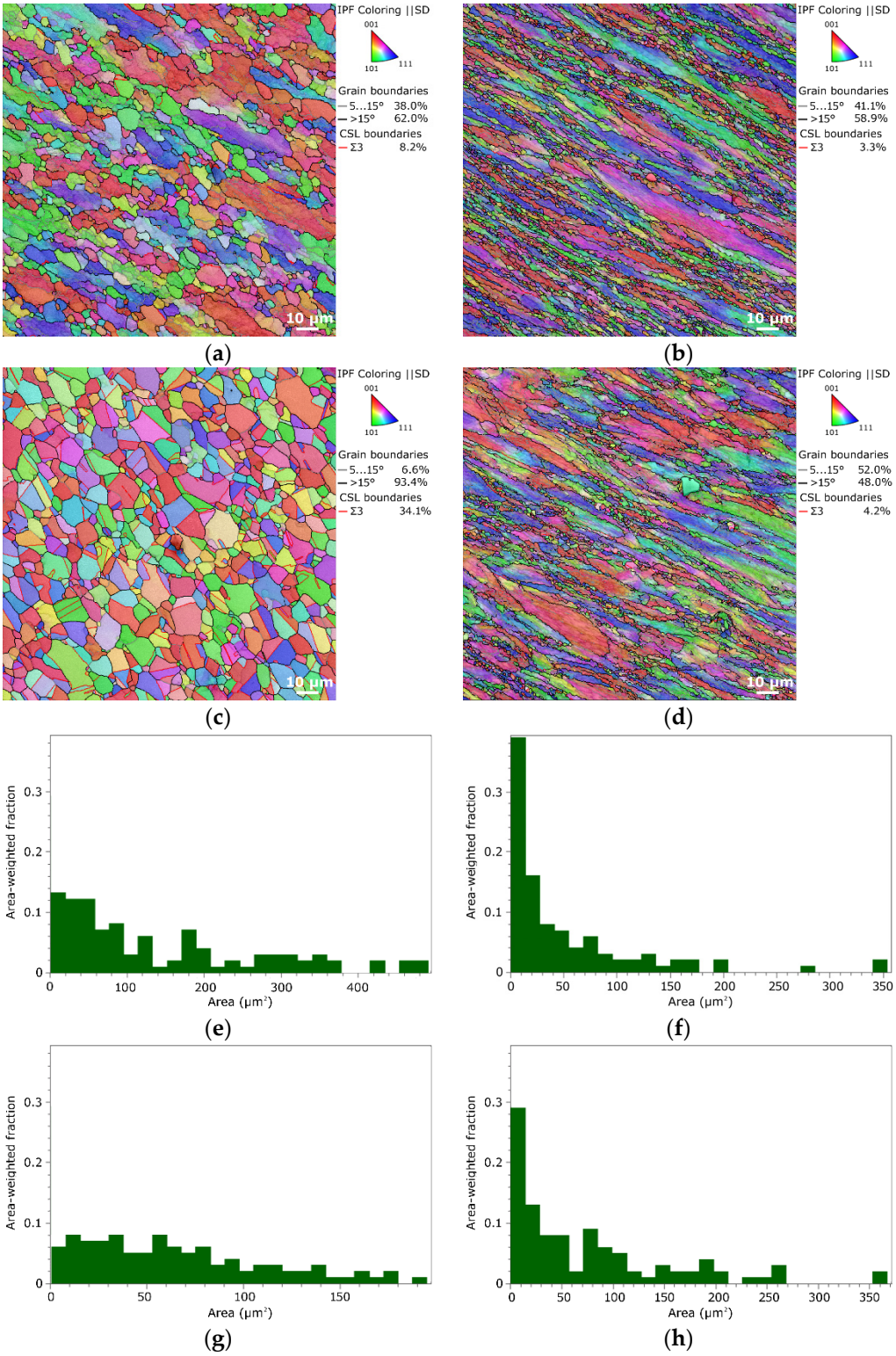

Figure 5. OIM images for 08Ch18N10T steel deformed under specific conditions: 1060 °C, 0.1 s^{-1} (**a**); 900 °C, 0.1 s^{-1} (**b**); 1060 °C, 10 s^{-1} (**c**); 900 °C, 10 s^{-1} (**d**). Grain size depicted via area-weighted grain areas for 08Ch18N10T steel deformed under specific conditions: 1060 °C, 0.1 s^{-1} (**e**); 900 °C, 0.1 s^{-1} (**f**); 1060 °C, 10 s^{-1} (**g**); 900 °C, 10 s^{-1} (**h**).

4. Discussion

The hot compression tests performed for the two selected austenitic steels provided valuable insights into their mechanical behaviors at elevated temperatures. The stress–strain curves acquired for both the steels showed that the flow stress only increased up to the peak point and then gradually decreased, or remained more or less constant (i.e., steady-state was established). In other words, neither the ChN35VT nor the 08Ch18N10T steel generally exhibited any significant flow stress decrease after the peak point was reached. Therefore, the development of intensive softening during the deformation ongoing after reaching the peak stress value seemed to be aggravated for both the steels. This phenomenon can most probably be attributed to the additions of relatively high amounts of elements featuring higher melting temperature (especially Cr or W, see Table 1) in both the steels, which can not only promote precipitation, but also increases the activation energy of recrystallization and thus aggravates the development of this dynamic softening mechanism [71]. The ChN35VT steel generally exhibited higher true flow stress values compared to the 08Ch18N10T one under identical thermo-mechanical conditions. This difference could most probably again be attributed to certain differences in the chemical composition, the most prominent of which were the differences in the contents of W and Ti (see Table 1) [72]. W can be considered to have a major effect on the grain size, as the addition of 1 wt. % W was reported to reduce the austenite grain size of the steel deformed at temperatures above 950 °C substantially [73]. This conclusion is supported by the fact that the 08Ch18N10T steel exhibited larger average grain sizes than the ChN35VT steel for all the investigated thermo-mechanical conditions.

When the different processing conditions were compared, both the investigated steels exhibited similar behaviors as regards the microstructure development. However, certain differences could be seen. During deformation at lower temperatures, the grains of both the investigated steels were deformed and significantly elongated; see Figures 3b,d, 4b,d and 5b,d, acquired for the steels deformed at 900 °C. Deformation at this temperature thus evidently supported the development of deformation substructure [74], especially for the 08Ch18N10T steel. On the contrary, for higher deformation temperatures, the grains were equiaxed and more or less randomly oriented, see Figures 3a,c, 4a,c and 5a,c, acquired for the steels deformed at 1060 °C. It can thus be said that deformation temperatures above ~1000 °C promote the development of dynamic recrystallization regardless of the applied strain rate [71]. The results also showed that the higher the strain rate, the more intense the development of dynamic recrystallization within the steels. In other words, increasing the strain rate supported dynamic recrystallization. This effect was significant especially for the ChN35VT steel, for which the increase in the strain rate supported substantially the development of dynamic recrystallization even at lower temperatures. Dynamic recrystallization is typically promoted by higher temperatures and lower strain rates [71]. However, the situation can be more complicated if precipitation takes place, as precipitation is known to delay the recrystallization processes Nevertheless, as precipitation requires a nucleation time period to develop, higher strain rates can inhibit this process and thus promote dynamic recrystallization and vice versa, i.e., lower strain rates can support precipitation and thus delay dynamic recrystallization. The applied strain rate also influences significantly the fraction of the <111>60° grain boundaries, i.e., twin boundaries. The results of the microstructure observations showed that the occurrence of twin boundaries after deformation at the lower strain rate was negligible. This can be explained by the fact that lower strain rates support the dislocation slip deformation mechanism, while twinning is a deformation mechanism supported by higher strain rates and/or lower temperatures [75]. Therefore, the twinning deformation mechanism is supported when the dislocations movement is aggravated, i.e., when the dislocations are not provided with sufficient time to pass through the lattice.

The validity of the original Hensel-Spittel model, which is implemented in the rheology databases of a wide range of FEM (finite element method)-based software, is limited for predicting the deformation behaviors of the steels primarily at lower temperatures, for

which it corresponds well with the experimentally acquired data. Therefore, determining the Hensel-Spittel equation, which would be applicable even at elevated and high temperatures, does not only provide an easy flow stress prediction, but, at the same time, enables the broadening of the inbuilt rheology databases of various FEM simulation software. A shortcoming of the presented rheology model is, however, that the description of the strain–stress curves at high temperatures is still not completely accurate after the stress value drops and the steady state is reached. This limitation is related to the fact that the Hensel-Spittel model does not incorporate the independently calculated peak point coordinates; thus, it does not describe the areas before the peak and after the peak separately.

5. Conclusions

The presented research focused on the characterization of the influence of thermo-mechanical parameters, i.e., temperature and strain rate, on the deformation behavior, i.e., stress–strain curves, and the microstructures of the ChN35VT and 08Ch18N10T austenitic stainless steels. The acquired experimental results were also used to determine the Hensel-Spittel rheology laws. Through a comprehensive analysis of the experimental results and subsequent discussions, the following key findings emerged:

- The ChN35VT steel showed higher flow stress values than the 08Ch18N10T steel;
- The 08Ch18N10T steel exhibited a larger grain size at all the tested strain rates and temperatures (at both the strain rates, the grain size for the 08Ch18N10T steel was approx. doubled at 900 °C, and ~1.3 times larger at 1060 °C);
- The ChN35VT steel microstructure generally exhibited higher fractions of high-angle grain boundaries, which points to the development of dynamic recrystallization;
- The mathematical description of the experimental data via the Hensel-Spittel models provided satisfactory curve fits, especially at lower temperatures;
- The developed Hensel-Spittel rheology low for the ChN35VT steel was

$$\sigma = 0.12 \cdot \mathrm{e}^{-0.005 \cdot T} \cdot T^{1.94} \cdot \varepsilon^{0.27} \cdot \mathrm{e}^{-0.005/\varepsilon} \cdot (1+\varepsilon)^{-0.001 \cdot T} \cdot \mathrm{e}^{0.13 \cdot \varepsilon} \cdot \dot{\varepsilon}^{-0.22} \cdot \dot{\varepsilon}^{0.0003 \cdot T};$$

- The developed Hensel-Spittel rheology low for the 08Ch18N10T steel was

$$\sigma = 1.66 \cdot 10^{8} \cdot \mathrm{e}^{-0.001 \cdot T} \cdot T^{-1.74} \cdot \varepsilon^{0.18} \cdot \mathrm{e}^{-0.02/\varepsilon} \cdot (1+\varepsilon)^{-0.001 \cdot T} \cdot \mathrm{e}^{0.29 \cdot \varepsilon} \cdot \dot{\varepsilon}^{-0.36} \cdot \dot{\varepsilon}^{0.0005 \cdot T}$$

Author Contributions: Conceptualization, methodology, L.K.; software, P.O.; investigation, J.N., L.K. and P.O.; data curation, J.N., P.O., L.K. and K.D.; writing—original draft preparation, J.N., L.K. and P.O.; writing—review and editing, L.K.; supervision, L.K.; project administration, K.D.; funding acquisition, L.K., P.O. and K.D. All authors have read and agreed to the published version of the manuscript.

Funding: This research was supported by the project number SP2023/022 of the VŠB–Technical University of Ostrava.

Data Availability Statement: The original data supporting the research are not publicly available, but a portion of the data that is not confidential is available on request from the corresponding author.

Conflicts of Interest: The authors declare no conflict of interest. The funders had no role in the design of the study; in the collection, analyses, or interpretation of the data; in the writing of the manuscript; or in the decision to publish the results.

References

1. Emelyanenko, K.A.; Emelyanenko, A.M.; Boinovich, L.B. Laser Obtained Superhydrophobic State for Stainless Steel Corrosion Protection, a Review. *Coatings* **2023**, *13*, 194. [CrossRef]
2. Astafurov, S.; Astafurova, E. Phase Composition of Austenitic Stainless Steels in Additive Manufacturing: A Review. *Metals* **2021**, *11*, 1052. [CrossRef]

3. Babaev, A.; Promakhov, V.; Schulz, N.; Semenov, A.; Bakhmat, V.; Vorozhtsov, A. Processes of Physical Treatment of Stainless Steels Obtained by Additive Manufacturing. *Metals* **2022**, *12*, 1449. [CrossRef]
4. Kunčická, L.; Kocich, R.; Lowe, T.C. Advances in Metals and Alloys for Joint Replacement. *Prog. Mater. Sci.* **2017**, *88*, 232–280. [CrossRef]
5. Butler-Smith, P.; See, T.; Humphrey, E.; Vilar, J.G.; Steege, T.; Kunze, T.; Schell, F.; Serey, N.; Tomic, D. A Comparison of the Tactile Friction and Cutting Performance of Textured Scalpel Blades Modified by Direct Laser Writing and Direct Laser Interference Patterning Processes. *Procedia CIRP* **2022**, *111*, 657–661. [CrossRef]
6. Zach, L.; Kunčická, L.; Růžička, P.; Kocich, R. Design, Analysis and Verification of a Knee Joint Oncological Prosthesis Finite Element Model. *Comput. Biol. Med.* **2014**, *54*, 53–60. [CrossRef]
7. Bračič, M.; Potrč, S.; Finšgar, M.; Gradišnik, L.; Maver, U.; Budasheva, H.; Korte, D.; Franko, M.; Fras Zemljič, L. Amoxicillin Doped Hyaluronic Acid/Fucoidan Multifunctional Coatings for Medical Grade Stainless Steel Orthopedic Implants. *Appl. Surf. Sci.* **2023**, *611*, 155621. [CrossRef]
8. Song, Y.L.; Yu, N.; Tan, D.B.P.; Chew, M.T. A Pilot Study on Three-Dimensional Printing of Stainless Steel Arch Bars for Orthognathic Segmental Jaw Surgeries. *Ann. 3D Print. Med.* **2022**, *6*, 100055. [CrossRef]
9. Fu, J.; Su, Y.; Qin, Y.-X.; Zheng, Y.; Wang, Y.; Zhu, D. Evolution of Metallic Cardiovascular Stent Materials: A Comparative Study among Stainless Steel, Magnesium and Zinc. *Biomaterials* **2020**, *230*, 119641. [CrossRef]
10. He, R.; Langi, E.; Garrard, R.; Attallah, M.M.; Silberschmidt, V.V.; Vogt, F.; Zhao, L. In Silico Evaluation of Additively Manufactured 316L Stainless Steel Stent in a Patient-Specific Coronary Artery. *Med. Eng. Phys.* **2022**, *109*, 103909. [CrossRef]
11. Kocich, R.; Kursa, M.; Szurman, I.; Dlouhý, A. The Influence of Imposed Strain on the Development of Microstructure and Transformation Characteristics of Ni–Ti Shape Memory Alloys. *J. Alloys Compd.* **2011**, *509*, 2716–2722. [CrossRef]
12. Xiuqing, X.; Junwei, A.; Chen, W.; Jing, N. Study on the Hydrogen Embrittlement Susceptibility of AISI 321 Stainless Steel. *Eng. Fail. Anal.* **2021**, *122*, 105212. [CrossRef]
13. Mankari, K.; Acharyya, S.G. Failure Analysis of AISI 321 Stainless Steel Welded Pipes in Solar Thermal Power Plants. *Eng. Fail. Anal.* **2018**, *86*, 33–43. [CrossRef]
14. Lee, S.K.; Yun, S.-H.; Joo, H.G.G.; Noh, S.J. Deuterium Transport and Isotope Effects in Type 316L Stainless Steel at High Temperatures for Nuclear Fusion and Nuclear Hydrogen Technology Applications. *Curr. Appl. Phys.* **2014**, *14*, 1385–1388. [CrossRef]
15. Fan, Y.; Liu, T.G.; Xin, L.; Han, Y.M.; Lu, Y.H.; Shoji, T. Thermal Aging Behaviors of Duplex Stainless Steels Used in Nuclear Power Plant: A Review. *J. Nucl. Mater.* **2021**, *544*, 152693. [CrossRef]
16. Vikulin, A.V.; Yaroslavtsev, N.L.; Zemlyanaya, V.A. Investigation into Transpiration Cooling of Blades in High-Temperature Gas Turbines. *Therm. Eng.* **2019**, *66*, 397–401. [CrossRef]
17. Kocich, R.; Bojko, M.; Macháčková, A.; Klečková, Z. Numerical Analysis of the Tubular Heat Exchanger Designed for Co-Generating Units on the Basis of Microturbines. *Int. J. Heat Mass Transf.* **2012**, *55*, 5336–5342. [CrossRef]
18. Macháčková, A.; Kocich, R.; Bojko, M.; Kunčická, L.; Polko, K. Numerical and Experimental Investigation of Flue Gases Heat Recovery via Condensing Heat Exchanger. *Int. J. Heat Mass Transf.* **2018**, *124*, 1321–1333. [CrossRef]
19. Ivanov, Y.F.; Petrikova, E.A.; Teresov, A.D.; Ivanova, O.V. High Chrome Steel Modified by High-Current Pulsed Electron Beam. *Russ. Phys. J.* **2020**, *62*, 2081–2085. [CrossRef]
20. Lin, K.; Qiao, J.; Gu, D.; Wang, H.; Shi, B.; Zhang, W.; Shan, J.; Xu, Y.; Tian, L. Active Screen Plasma Nitriding of Laser Powder Bed Fusion Processed 316L Stainless Steel for the Application of Fuel Cell Bipolar Plates. *Virtual Phys. Prototyp.* **2023**, *18*, e2225490. [CrossRef]
21. Chen, H.; Li, W.; Chen, W.; Chen, J.; Zhang, S. Influence of Prior Creep-Fatigue Exposure on Remnant Tensile and Creep Properties of AISI 321 Austenite Stainless Steel. *Int. J. Fatigue* **2022**, *159*, 106826. [CrossRef]
22. Wang, J.; Su, H.; Chen, K.; Du, D.; Zhang, L.; Shen, Z. Effect of δ-Ferrite on the Stress Corrosion Cracking Behavior of 321 Stainless Steel. *Corros. Sci.* **2019**, *158*, 108079. [CrossRef]
23. Ghazani, M.S.; Eghbali, B. Characterization of the Hot Deformation Microstructure of AISI 321 Austenitic Stainless Steel. *Mater. Sci. Eng. A* **2018**, *730*, 380–390. [CrossRef]
24. Zhao, D.; Ren, L.; Wang, Y.; Wang, W.; Zhu, Z.; Fu, W. Hot Deformation Behaviors of as Cast 321 Austenitic Stainless Steel. *Metals* **2021**, *11*, 1245. [CrossRef]
25. Volgina, N.; Shulgin, A.; Khlamkova, S. Possibilities of Diagnosis of Stress Corrosion Cracking of Main Gas Pipelines from the Point of View of Microbiology. *Mater. Today Proc.* **2021**, *38*, 1697–1700. [CrossRef]
26. Bykova, A.E.; Sharipzyanova, G.K.; Volgina, N.I.; Khlamkova, S.S. Methodology of Analyzing the Causes of Accidental Failure of Pipes Made of Various Steel Grades. *Russ. Metall.* **2018**, *2018*, 1264–1267. [CrossRef]
27. Yang, L.; Webler, B.A.; Cheng, G. Precipitation Behavior of Titanium Nitride on a Primary Inclusion Particle during Solidification of Bearing Steel. *J. Iron Steel Res. Int.* **2017**, *24*, 685–690. [CrossRef]
28. Chabaud-Reytier, M.; Allais, L.; Caes, C.; Dubuisson, P.; Pineau, A. Mechanisms of Stress Relief Cracking in Titanium Stabilised Austenitic Stainless Steel. *J. Nucl. Mater.* **2003**, *323*, 123–137. [CrossRef]
29. Zhang, W.; Wu, J.; Wen, Y.; Ye, J.; Li, N. Characterization of Different Work Hardening Behavior in AISI 321 Stainless Steel and Hadfield Steel. *J. Mater. Sci.* **2010**, *45*, 3433–3437. [CrossRef]

30. Pardo, A.; Merino, M.C.; Coy, A.E.; Viejo, F.; Carboneras, M.; Arrabal, R. Influence of Ti, C and N Concentration on the Intergranular Corrosion Behaviour of AISI 316Ti and 321 Stainless Steels. *Acta Mater.* **2007**, *55*, 2239–2251. [CrossRef]
31. Shabashov, V.; Lyashkov, K.; Zamatovskii, A.; Kozlov, K.; Kataeva, N.; Novikov, E.; Ustyugov, Y. Mechanosynthesis of High-Nitrogen Steels Strengthened by Secondary Titanium Nitrides. *Materials* **2022**, *15*, 5038. [CrossRef] [PubMed]
32. Torres, C.; Hazarabedian, M.S.; Quadir, Z.; Johnsen, R.; Iannuzzi, M. The Role of Tungsten on the Phase Transformation Kinetics and Its Correlation with the Localized Corrosion Resistance of 25Cr Super Duplex Stainless Steels. *J. Electrochem. Soc.* **2020**, *167*, 081510. [CrossRef]
33. Lo, K.H.; Shek, C.H.; Lai, J.K.L. Recent Developments in Stainless Steels. *Mater. Sci. Eng. R Rep.* **2009**, *65*, 39–104. [CrossRef]
34. Torres, N.; Greivel, G.; Betz, J.; Moreno, E.; Newman, A.; Thomas, B. Optimizing Steel Coil Production Schedules under Continuous Casting and Hot Rolling. *Eur. J. Oper. Res.* **2023**, *in press*. [CrossRef]
35. Lukáč, P.; Kocich, R.; Greger, M.; Padalka, O.; Szaraz, Z. Microstructure of AZ31 and AZ61 Mg Alloys Prepared by Rolling and ECAP. *Kov. Mater. Mater.* **2007**, *45*, 115–120.
36. Chichenev, N.A.; Vasilyev, M.V.; Karfidov, A.O.; Chicheneva, O.N. Device for Two-Way Cooling of Rolls of Multi-Roll Mills during Laser Hardening. *CIS Iron Steel Rev.* **2023**, *25*, 46–50. [CrossRef]
37. Silva, V.M.A.; Camerini, C.G.; Pardal, J.M.; de Blás, J.C.G.; Pereira, G.R. Eddy Current Characterization of Cold-Worked AISI 321 Stainless Steel. *J. Mater. Res. Technol.* **2018**, *7*, 395–401. [CrossRef]
38. Seval'neva, T.G.; Terent'ev, V.F.; Seval'nev, G.S.; Vlasov, I.I. Structure Formation in a Wire Made of Austenitic–Martensitic VNS9-Sh TRIP Steel during Drawing. *Russ. Metall.* **2021**, *2021*, 1270–1274. [CrossRef]
39. Xu, Q.; Zhu, J.; Zong, Y.; Liu, L.; Zhu, X.; Zhang, F.; Luan, B. Effect of Drawing and Annealing on the Microstructure and Mechanical Properties of 304 Austenitic Stainless Steel Wire. *Mater. Res. Express* **2021**, *8*, 126530. [CrossRef]
40. Vermes, B.; Czigany, T. Non-Conventional Deformations: Materials and Actuation. *Materials* **2020**, *13*, 1383. [CrossRef]
41. Macháčková, A.; Krátká, L.; Petrmichl, R.; Kunčická, L.; Kocich, R. Affecting Structure Characteristics of Rotary Swaged Tungsten Heavy Alloy Via Variable Deformation Temperature. *Materials* **2019**, *12*, 4200. [CrossRef] [PubMed]
42. Kunčická, L.; Kocich, R. Optimizing Electric Conductivity of Innovative Al-Cu Laminated Composites via Thermomechanical Treatment. *Mater. Des.* **2022**, *215*, 110441. [CrossRef]
43. Kocich, R. Design and Optimization of Induction Heating for Tungsten Heavy Alloy Prior to Rotary Swaging. *Int. J. Refract. Met. Hard Mater.* **2020**, *93*, 105353. [CrossRef]
44. Thomasová, M.; Seiner, H.; Sedlák, P.; Frost, M.; Ševčík, M.; Szurman, I.; Kocich, R.; Drahokoupil, J.; Šittner, P.; Landa, M. Evolution of Macroscopic Elastic Moduli of Martensitic Polycrystalline NiTi and NiTiCu Shape Memory Alloys with Pseudoplastic Straining. *Acta Mater.* **2017**, *123*, 146–156. [CrossRef]
45. Xu, Z.; Zhang, H.; Krishnan, P.; Hale, C.; Kecskes, L.J.; Yarmolenko, S.; Fialkova, S.; Wei, Q.; Sankar, J. Non-Conventional Hot Rolling for Improvement of Mechanical Properties in Binary Mg-Alloys. *Mech. Mater.* **2022**, *164*, 104111. [CrossRef]
46. Kocich, R.; Macháčková, A.; Fojtík, F. Comparison of Strain and Stress Conditions in Conventional and ARB Rolling Processes. *Int. J. Mech. Sci.* **2012**, *64*, 54–61. [CrossRef]
47. Kocich, R.; Greger, M.; Macháčková, A. Finite Element Investigation of Influence of Selected Factors on ECAP Process. In Proceedings of the METAL 2010: 19th International Metallurgical and Materials Conference, Roznov pod Radhostem, Czech Republic, 18–20 May 2010; Tanger Ltd.: Ostrava, Czech Republic, 2010; pp. 166–171.
48. Kocich, R.; Kursa, M.; Macháčková, A. FEA of Plastic Flow in AZ63 Alloy during ECAP Process. *Acta Phys. Pol. A* **2012**, *122*, 581–587. [CrossRef]
49. Hlaváč, L.M.; Kocich, R.; Gembalová, L.; Jonšta, P.; Hlaváčová, I.M. AWJ Cutting of Copper Processed by ECAP. *Int. J. Adv. Manuf. Technol.* **2016**, *86*, 885–894. [CrossRef]
50. Kocich, R.; Fiala, J.; Szurman, I.; Macháčková, A.; Mihola, M. Twist-Channel Angular Pressing: Effect of the Strain Path on Grain Refinement and Mechanical Properties of Copper. *J. Mater. Sci.* **2011**, *46*, 7865–7876. [CrossRef]
51. Kocich, R.; Kunčická, L.; Král, P.; Macháčková, A. Sub-Structure and Mechanical Properties of Twist Channel Angular Pressed Aluminium. *Mater. Charact.* **2016**, *119*, 75–83. [CrossRef]
52. Kocich, R.; Kunčická, L.; Macháčková, A. Twist Channel Multi-Angular Pressing (TCMAP) as a Method for Increasing the Efficiency of SPD. *IOP Conf. Ser. Mater. Sci. Eng.* **2014**, *63*, 012006. [CrossRef]
53. Naizabekov, A.B.; Andreyachshenko, V.A.; Kocich, R. Study of Deformation Behavior, Structure and Mechanical Properties of the AlSiMnFe Alloy during ECAP-PBP. *Micron* **2013**, *44*, 210–217. [CrossRef] [PubMed]
54. Kong, D.; Ni, X.; Dong, C.; Zhang, L.; Man, C.; Yao, J.; Xiao, K.; Li, X. Heat Treatment Effect on the Microstructure and Corrosion Behavior of 316L Stainless Steel Fabricated by Selective Laser Melting for Proton Exchange Membrane Fuel Cells. *Electrochim. Acta* **2018**, *276*, 293–303. [CrossRef]
55. Hemmasian Ettefagh, A.; Guo, S.; Raush, J. Corrosion Performance of Additively Manufactured Stainless Steel Parts: A Review. *Addit. Manuf.* **2021**, *37*, 101689. [CrossRef]
56. Saboori, A.; Aversa, A.; Marchese, G.; Biamino, S.; Lombardi, M.; Fino, P. Microstructure and Mechanical Properties of AISI 316L Produced by Directed Energy Deposition-Based Additive Manufacturing: A Review. *Appl. Sci.* **2020**, *10*, 3310. [CrossRef]
57. Vaičiukynienė, D.; Jakevičius, L.; Kantautas, A.; Vaitkevičius, V.; Vaičiukynas, V.; Dvořák, K. Conversion of Silica By-Product into Zeolites by Thermo-Sonochemical Treatment. *Ultrason. Sonochem.* **2021**, *72*, 105426. [CrossRef]

58. Shakil, S.I.; Smith, N.R.; Yoder, S.P.; Ross, B.E.; Alvarado, D.J.; Hadadzadeh, A.; Haghshenas, M. Post Fabrication Thermomechanical Processing of Additive Manufactured Metals: A Review. *J. Manuf. Process.* **2022**, *73*, 757–790. [CrossRef]
59. Kunčická, L.; Kocich, R.; Németh, G.; Dvořák, K.; Pagáč, M. Effect of Post Process Shear Straining on Structure and Mechanical Properties of 316 L Stainless Steel Manufactured via Powder Bed Fusion. *Addit. Manuf.* **2022**, *59*, 103128. [CrossRef]
60. Li, W.; Chen, H.; Huang, W.; Chen, J.; Zuo, L.; Li, C.; He, J.; Ren, Y.; Zhang, S. Effect of Laser Shock Peening on High Cycle Fatigue Properties of Aluminized AISI 321 Stainless Steel. *Int. J. Fatigue* **2021**, *147*, 106180. [CrossRef]
61. Song, S.-H. A Comparison Study of Constitutive Equation, Neural Networks, and Support Vector Regression for Modeling Hot Deformation of 316L Stainless Steel. *Materials* **2020**, *13*, 3766. [CrossRef]
62. Li, W.; Chen, H.; Huang, W.; Chen, J.; Li, C.; Xu, D.; An, S.; Zhang, S.; Yang, H. High-Temperature Creep Property and Life Prediction of Aluminized AISI 321 Stainless Steel after Annealing Diffusion Treatment. *Eng. Fail. Anal.* **2021**, *128*, 105611. [CrossRef]
63. Radionova, L.V.; Perevozchikov, D.V.; Makoveckii, A.N.; Eremin, V.N.; Akhmedyanov, A.M.; Rushchits, S.V. Study on the Hot Deformation Behavior of Stainless Steel AISI 321. *Materials* **2022**, *15*, 4057. [CrossRef] [PubMed]
64. Savaedi, Z.; Motallebi, R.; Mirzadeh, H. A Review of Hot Deformation Behavior and Constitutive Models to Predict Flow Stress of High-Entropy Alloys. *J. Alloys Compd.* **2022**, *903*, 163964. [CrossRef]
65. Motallebi, R.; Savaedi, Z.; Mirzadeh, H. Additive Manufacturing—A Review of Hot Deformation Behavior and Constitutive Modeling of Flow Stress. *Curr. Opin. Solid State Mater. Sci.* **2022**, *26*, 100992. [CrossRef]
66. Kunčická, L.; Kocich, R.; Drápala, J.; Andreyachshenko, V.A. FEM Simulations and Comparison of the Ecap and ECAP-PBP Influence on Ti6Al4V Alloy's Deformation Behaviour. In Proceedings of the METAL 2013: 22nd International Metallurgical and Materials Conference, Brno, Czech Republic, 15–17 May 2013; Tanger Ltd.: Ostrava, Czech Republic, 2013; pp. 391–396.
67. Kocich, R.; Macháčková, A.; Kunčická, L. Twist Channel Multi-Angular Pressing (TCMAP) as a New SPD Process: Numerical and Experimental Study. *Mater. Sci. Eng. A* **2014**, *612*, 445–455. [CrossRef]
68. Kocich, R.; Kunčická, L.; Mihola, M.; Skotnicová, K. Numerical and Experimental Analysis of Twist Channel Angular Pressing (TCAP) as a SPD Process. *Mater. Sci. Eng. A* **2013**, *563*, 86–94. [CrossRef]
69. Al-Areeq, A.M.; Saleh, R.A.A.; Ghanim, A.A.J.; Ghaleb, M.; Al-Areeq, N.M.; Al-Wajih, E. Flood Hazard Assessment in Yemen Using a Novel Hybrid Approach of Grey Wolf and Levenberg Marquardt Optimizers. *Geocarto Int.* **2023**, *38*, 2243884. [CrossRef]
70. Chen, J.; Jiang, Z.; Que, Y. Hierarchical Recursive Levenberg–Marquardt Algorithm for Radial Basis Function Autoregressive Models. *Inf. Sci.* **2023**, *647*, 119506. [CrossRef]
71. Humphreys, F.J.; Hetherly, M.; Rollett, A.; Rohrer, G.S. *Recrystallization and Related Annealing Phenomena*, 2nd ed.; Elsevier Ltd.: Oxford, UK, 2004; ISBN 008-044164-5.
72. Ahssi, M.A.M.; Erden, M.A.; Acarer, M.; Çuğ, H. The Effect of Nickel on the Microstructure, Mechanical Properties and Corrosion Properties of Niobium–Vanadium Microalloyed Powder Metallurgy Steels. *Materials* **2020**, *13*, 4021. [CrossRef]
73. Zhao, J.; Lee, T.; Lee, J.H.; Jiang, Z.; Lee, C.S. Effects of Tungsten Addition on the Microstructure and Mechanical Properties of Microalloyed Forging Steels. *Metall. Mater. Trans. A* **2013**, *44*, 3511–3523. [CrossRef]
74. Salehi, M.; Yeganeh, M.; Heidari, R.B.; Eskandari, M. Comparison of the Microstructure, Corrosion Resistance, and Hardness of 321 and 310s Austenitic Stainless Steels after Thermo-Mechanical Processing. *Mater. Today Commun.* **2022**, *31*, 103638. [CrossRef]
75. Verlinden, B.; Driver, J.; Samajdar, I.; Doherty, R.D. *Thermo-Mechanical Processing of Metallic Materials*; Elsevier: Amsterdam, The Netherlands, 2007; ISBN 9780080444970.